Opto-Electronic Advances

CN 51-1781/TN ISSN 2096-4579 (Print) ISSN 2097-3993 (Online)

Halide perovskite volatile unipolar nanomemristor

Abolfazl Mahmoodpoor, Prokhor A. Alekseev, Ksenia A. Gasnikova, Kuzmenko Natalia, Artem Larin, Sergey Makarov and Aleksandra Furasova

Citation: Mahmoodpoor A, Alekseev PA, Gasnikova KA, et al. Halide perovskite volatile unipolar nanomemristor. *Opto-Electron Adv* **8**, 250110(2025).

https://doi.org/10.29026/oea.2025.250110

Received: 13 May 2025; Accepted: 28 July 2025; Published online: 15 October 2025

Opto-Electronic Advances

Article

November 2025, Vol. 8, No. 11

DOI: 10.29026/oea.2025.250110 CSTR: 32247.14.oea.2025.250110

Halide perovskite volatile unipolar nanomemristor

Abolfazl Mahmoodpoor[1,2†], Prokhor A. Alekseev[2,3†], Ksenia A. Gasnikova[2,3], Kuzmenko Natalia[4], Artem Larin[2], Sergey Makarov[1,2*] and Aleksandra Furasova[1,2*]

Halide perovskites is a recently emerged platform for the creation of efficient memristors. In turn, single-crystal inorganic perovskite would be new low-cost and flexible memory devices because of their excellent resistive switching (RS) properties, without risk of chemical and mechanical stress-generated degradation, compared with the operational instability of general thin-film perovskite memristors. Moreover, miniaturization of perovskite memristors would be useful for creating high-density memory devices. Here we demonstrate the smallest $CsPbBr_3$ perovskite nanomemristor with volatile unipolar RS characteristics which depends on the size of a single-crystal as a resistive layer due to its overall structural stability and low sensitivity to atmosphere conditions that helps to keep the stable RS switching over 1500 times with the lowest consumption power of 70 nW. To better understand the RS mechanism, we provide a comprehensive simulation of the evolution of mixed ionic-electronic charge carriers under current-voltage (*I*-*V*) tests using a one-dimensional drift-diffusion model. Because of the nonreactive nature of the contacts, the main mechanism of resistive state switching is potential barrier modulation of the Schottky contacts through the accumulation of migrating ions at the interfaces. Our findings pave the way for ultracompact memristors as well as shed light on RS mechanism in non-filamentary perovskite-based memory devices.

Keywords: perovskite nanocrystals; nanomemristor; volatile memory; resistive switching; ions migration

Mahmoodpoor A, Alekseev PA, Gasnikova KA et al. Halide perovskite volatile unipolar nanomemristor. *Opto-Electron Adv* **8**, 250110 (2025).

Introduction

The emergence of memristors has revolutionized the field of non-volatile memory and neuromorphic computing[1,2], offering a promising avenue for the development of energy-efficient computing. Among the various materials explored for memristor applications[3–5], halide perovskite crystals were attracted significant attention due to their bipolar carrier transport, high electronic charge carrier mobility, unique electrical and optical properties, and simplicity of fabrication[6–9]. The RS mechanisms in perovskite memristors were thoroughly analyzed by classifying them into two distinct models: the conductive filament (CF) model and the interface modulation of charge carrier injection. In the CF model, bipolar switching is a fundamental requirement for achieving RS. The primary mechanism underlying

[1]Qingdao Innovation and Development Center, Harbin Engineering University, Qingdao 266000, China; [2]ITMO University, School of Physics and Engineering, Kronverkskiy pr. 49, 197101, St. Petersburg, Russia; [3]Ioffe Institute, 194021 Polytechnicheskaya 26, St. Petersburg, Russia; [4]ITMO University, Research Center for Optical Materials Science, Kronverkskiy pr. 49, 197101, St. Petersburg, Russia.

†These authors contributed equally to this work.

*Correspondence: S Makarov, E-mail: s.makarov@metalab.ifmo.ru; A Furasova, E-mail: aleksandra.furasova@metalab.ifmo.ru

Received: 13 May 2025; Accepted: 28 July 2025; Published online: 15 October 2025

filament formation in ABX_3 perovskites involves oxidation-reduction (redox) reactions of contact metals such as Cu and Ag[10], along with the migration of metallic cations. When a positive voltage is applied, the metallic element undergoes oxidation, resulting in the formation of cations that migrate toward the opposite electrode. Upon reaching the counter electrode, these cations are neutralized, forming neutral atoms that accumulate and grow towards the positive electrode, leading to the establishment of a metallic CF through the whole perovskite memristor[11]. At this stage, the system converts to a low resistive state (LRS). The application of a reducing potential does not alter the state of the device until a negative bias is applied to the reactive metallic contact. When reverse bias is applied from zero to high voltage, the conductive filaments should dissolve and break apart as a result of redox reactions, causing the device to revert from LRS to a high-resistive state (HRS).

In contrast, in non-filamentary base memory devices, the modulation of the charge carrier injection is influenced by the applied bias, whether a positive or negative bias is applied to contacts, and RS can occur under unipolar conditions[12]. Specifically, the presence of mobile ions in perovskite semiconductors[13–15] means that increasing the bias results in a greater accumulation of these ions at the perovskite-contact interface. This accumulation can alter the depletion width of the Schottky contact, making it either narrower or wider. Consequently, the density of ions at the interface can significantly impact carrier tunneling and Schottky barrier lowering. Several groups reported interface-based modulation phenomena as the mechanism for RS[16,17]. In a work by Han et al.[18], it is proposed that the accumulation of tin vacancies at the interface between gold and cesium tin iodide perovskite leads to a reduction in the depletion width, which in turn enhances carrier tunneling. Therefore, since carrier tunneling depends on the concentration of ions, and this ion concentration varies with the applied bias, the RS mechanism is consequently influenced by the amplitude of the applied bias. Conversely, in the CF model of RS, the polarity of the applied bias plays a crucial role in the formation and rupture of filaments, which govern changes in resistivity. The essential difference in a non-filamentary RS mechanism is that, because it relies on ion redistribution rather than redox reactions as in the CF model, it can lead to improved material stability and cycle endurance.

Despite many papers[19–22] reported about CF formation in thin film perovskite memristors with metal contact, it is still difficult to tell confidently about stable electric characteristics of these devices under high-voltage load. Although some perovskite-based devices with metallic electrodes exhibit low stability under varying environmental conditions such as oxidation at room humidity and temperature-assisted penetration of metal ions through various charge transport layers[23], several other significant challenges must be addressed in the development of perovskite-based memristors. Key issues include cycling endurance, switching ratio optimization, power consumption reduction, and miniaturization. Another problem is the understanding of the underlying switching mechanisms, and more research is needed to elucidate the role of defects and ion migration in the performance of perovskite memristors.

In this study, we present for the first time a simple solution to create a ultracompact perovskite memristor with a stable unipolar RS mechanism based on carrier injection modulation in a single $CsPbBr_3$ nanocrystal. For this purpose, we synthesized the nanocrystals with sizes in the range 10^1–10^2 nm on an indium tin oxide (ITO) substrate and record stable cyclic voltammograms over 1000 cycles by probing the current with a boron-doped diamond (BDD) tip of an atomic force microscope (AFM) as a top contact. Our findings reveal that the V_{SET}/V_{RESET} potentials, which are threshold potentials for altering the device's resistivity from high to low and vice versa, respectively, can be effectively controlled by adjusting the size of the single nanocrystals. This phenomenon aligns with previous works dedicated to the creation of a single-layer thin-film based perovskite memristors[24], demonstrated RS behavior in an organic-inorganic hybrid $CH_3NH_3PbI_{3-x}Cl_x$ perovskite deposited on an FTO/glass substrate with a metallic top contact, although their study was limited to only 100 stable cycles. In addition, we reveal that for relatively larger perovskite crystals (over 160 nm) RS has smooth behavior while for smaller single crystals RS is sharp and has a lower V_{SET}. Indeed, such small single-crystal-based memristors exhibit low operating current of 30–300 nA, low power consumption of 70–700 nW, switching time less than 1 ms, and current amplitude is about 4–5 orders of magnitude being strongly dependent on their size and described well by our model. Through numerical simulations, we investigate the dynamics of electronic and ionic carriers within a single perovskite nanocrystal. Our analysis reveals that, in addition to carrier tunneling

from the contacts, the reduction of the Schottky barrier due to image force charges, along with the dipole effect in barrier reduction, plays a crucial role in the measured *I-V* characteristics of the halide perovskite volatile unipolar nanomemristor.

Results and discussion

Single perovskite crystals have been synthesized with 2-step deposition method well described by Tiguntseva et al.[25] on an ITO crystal with resistance of 7 Ω/cm² where individual NPs do not have a trend sticking together, according to scanning electron microscopy (SEM) image (Fig. 1(b)). This method of synthesis on ITO surface has a number of benefits for fabrication of well crystalline nanocubes. In addition, the size of single cubes can be tuned with speed of spin coater and $PbBr_2$ concentration in DMF solution at the first step of the synthesis. The electron diffraction image obtained in a transmission electron microscope shows that each $CsPbBr_3$ particle is a single crystal and relates to a cubic structure of *Pm3m* symmetry with the following lattice parameters: $a = b = c = 0.5874$ nm, with angles of $\alpha = \beta = \gamma = 90°$[26]. If a crystal has 0.58 nm long planes, only a cube can be formed, since the total number of planes remains 6[27], which explains the fact that synthesized nanoparticles being over than 100 nm have a shape which is close to a cube. In addition, XRD analysis (Section S6) identifies $CsPbBr_3$ particle as a material with high crystalline quality. A typical broadband Raman spectra for $CsPbBr_3$ at room temperature is shown in Fig. 1(d), where, the peak at 125 cm^{-1} peak belongs to the third transverse optical (TO_3) phonon mode of $CsPbBr_3$[28] and 156 cm^{-1} peak is attributed to the symmetric Br-Pb-Br octahedral stretch[29] and the highest frequency mode 309 cm^{-1} [30].

To form conductive filaments in perovskite thin-film based memristors several studies reported the use of Ag contact to achieve Ag ion migration under applied bias[31–34]. Alongside the formation of cation-based filaments, anion-based filaments arise primarily from the migration of halide vacancies within the perovskite structure. In a study conducted by Li et al.[35], it was demonstrated that enhancing the migration barrier for bromine vacancies in $CsPb(Br_xI_{1-x})_3$ perovskite significantly improves the RS endurance, allowing for more

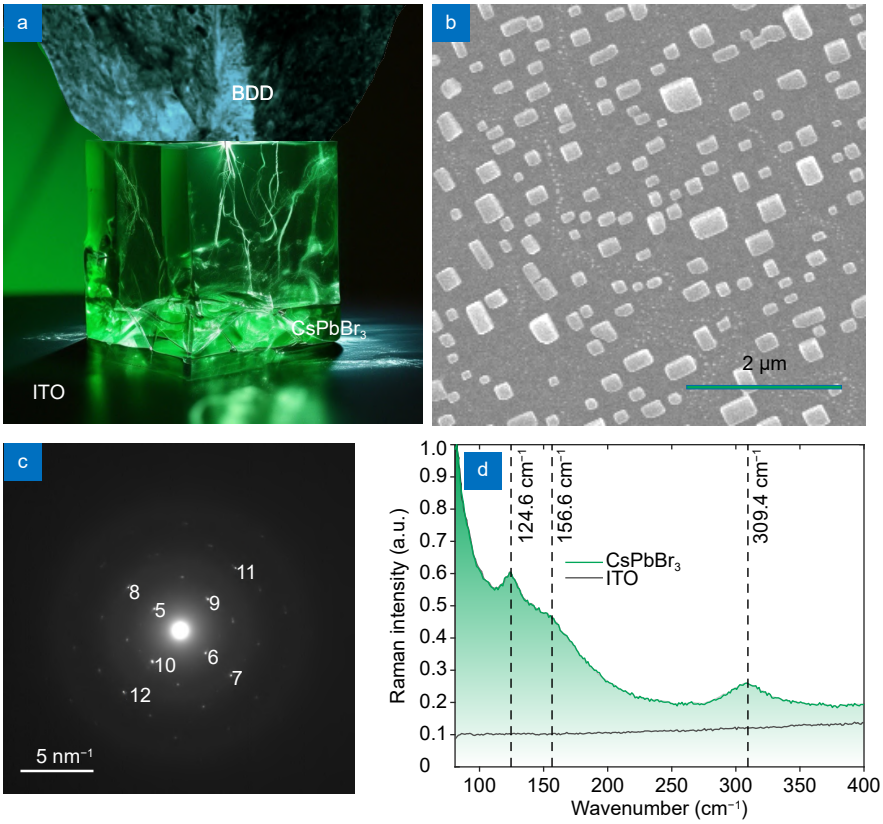

Fig. 1 | Principle of simple perovskite memory device, morphology and structural analysis. (**a**) A schematic illustration of a perovskite nanomemristor based on a single crystal on indium tin oxide (ITO) contacted with boron-doped diamond (BDD). (**b**) Scanning top view of the perovskite nanocrystals array. (**c**) Electron diffraction image of an individual $CsPbBr_3$ nanocrystal. (**d**) Raman spectra obtained from the single-crystals array.

than 100 cycles of operation. However, the long-term stability of this architecture is still under discussion. Emelianov et al. visualized methylammonium (MA^+) cation dynamics under an applied electric field and $MAPbI_3$ films degradation under 1 V when the perovskite film is connected directly with metal[19]. Moreover, it was shown that redox or degradation processes are usually uniform and do not have local states which are suppose to generate CFs[20,21]. Also, RS mechanism based on carrier tunneling from the Schottky barrier is reported in several works[17,36]. Furthermore, alongside the previously mentioned mechanisms of interface carrier injection modulation, several models emerged as particularly useful: the space charge limited current (SCLC) transport model[37,38], the negative differential resistance phenomenon[39] and a dynamical model based on an equivalent circuit for describing the characteristic *I-V* curve proposed by Berruet et al.[40]. A real strong CF observation was shown for thin imine polymer based on benzene-1,3,5-tricarbaldehyde and *p*-phenylenediamine monomers[22] with retention time of 10^3 second under a voltage bias of −0.1 V. It is more important that Liu et al.[22] demonstrated that the increase of the polymer thickness improves the LRS/RS current ratio.

To improve cycling endurance, Kim et al. proposed the incorporation of a transport layer, demonstrating that the addition of a TPBI electron transport layer between silver and perovskite significantly increased the number of cycles from 90 to 1000[41]. In another study, Yin et al. showed that integrating a zinc oxide (ZnO) layer at either the top or bottom electrode of the FTO/$CsPbBr_3$/Au structure improved the switching ratio from 10^3 to 10^5 [42]. To make our device simpler and more stable, we used both ion blocking contacts that help to avoid CF appearance and produce memristive states solely by ion and charge migration.

To measure *I-V* curves from a determined single particle, the area of a patterned ITO was first scanned by SEM to establish the lateral size: width and length, of the each individual crystal and then this place was scanned with AFM to correctly establish the height of the measured nanocube (Supplementary information Fig. S1). A special procedure of the tip apex cleaning (details are in the Section S1 of Supplementary information) was developed to ensure that an electrical contact is made between the bare probe's BDD and the particle of interest.

The tip of a BDD probe has a resistance of 100 kΩ and a size that is similar to the size of the cube side, thus, it can be considered as a fully covered contact. It is worth noting, that the employed probe has a relatively blunt tip that broadens perovskite nanoparticles in the AFM image (Fig. S1(b)). Additionally, during the measurements, some of the particles can be attached to the sides of the probe causing doubling or even tripling of topographical features in the AFM image.

The threshold voltage was determined by the first *I-V* curve, measured from zero to positive voltage within 50 ms. Note that the $V_{\mathrm{RESET/SET}}$ measured up to 3 V and 5 V on the same particle may differ, since when measuring from 0 V to 5 V, the particle was maintained for a shorter time in the pre-threshold voltage. Figure 2 shows the *I-V* characteristics of individual particles with different heights from 100 nm to 200 nm. In total, the height evaluated for $CsPbBr_3$ was in a range of 90–250 nm for the *I-V* measurements. For our device structure, the first *I-V* curve does not have significant difference from other scanned 998 cycles and stays with the same voltage switching potential from high-resistive to low-resistive states for a long time of the test. This behavior differs from other previous reports where the first scanning process generates conductive filaments and further *I-V* parameters are defined by the initial electroforming process[7]. Moreover, in generally prepared polycrystalline perovskite film-based memristors the overshoot current flows in parallel through the formed filaments and the whole perovskite film, which makes RS characteristics less reproducible and more fluctuating. In addition, if the quality of organic-inorganic perovskite films gets worse under ambient conditions of explosion, it will cause degradation of the off-state resistance with a long-term cycling.

In contrast, our systems have a stable RS behavior: the voltage gap between LRS and HRS (Set/Reset potential) switching remains constant after 200 cycles and does not collapse with time for particles larger than 110 nm. This Set/Reset window collapses with time for perovskite thin-film memristors if they have filaments that lead to accumulating of metallic Pb sites and becomes less rupture[43]. The device *I-V* characteristics and their stability from cycle to cycle are distinguished in current research because of the choice of a single inorganic perovskite nanocrystal as a semiconductor, which helps to avoid any perturbations that usually occur with a polycrystalline feature in flat perovskite thin films and makes them dependent on filament formation. A Set/Reset potential changes under 1500 *I-V* cycles of the single-particle

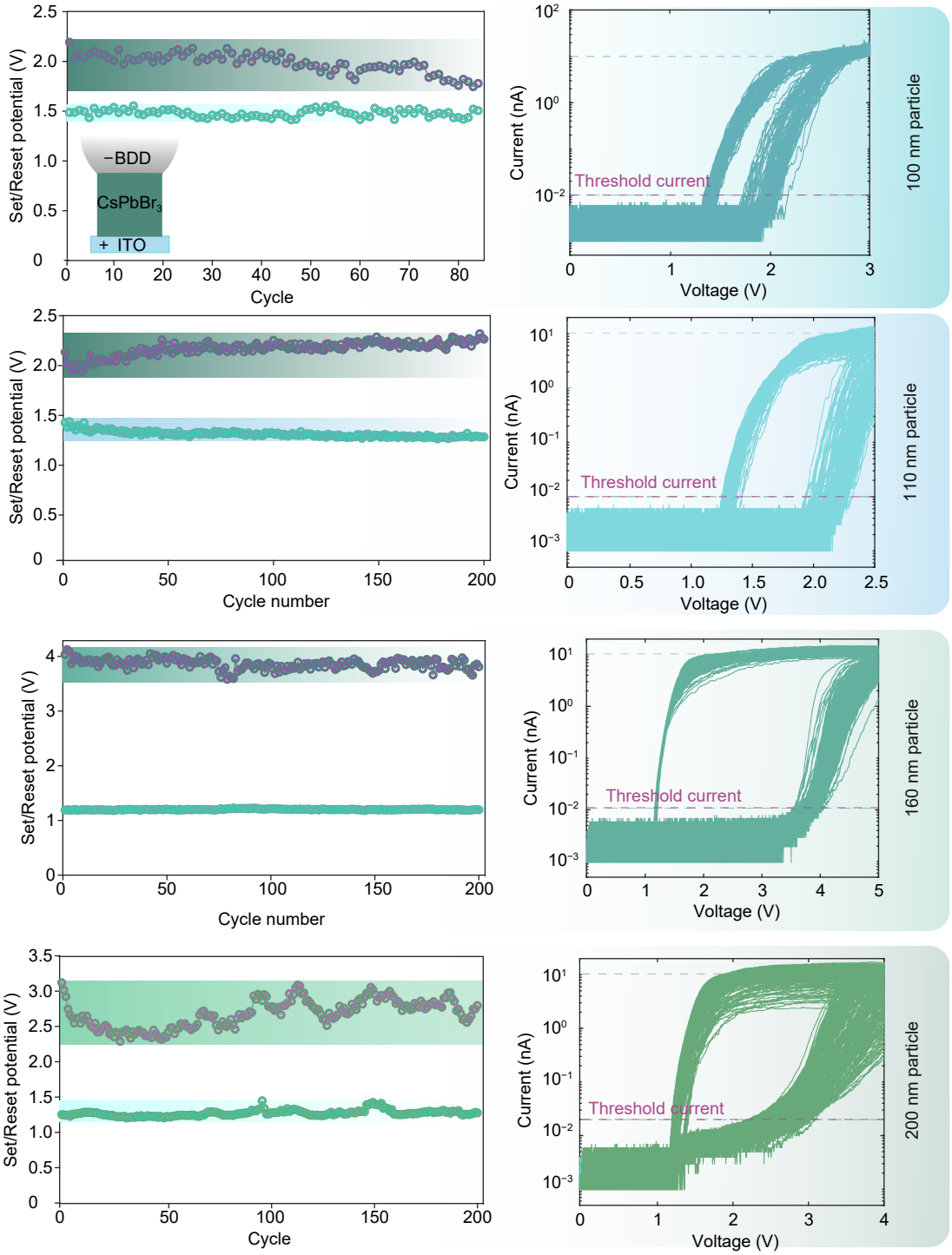

Fig. 2 | Electrical switching behavior of single crystal memristors with different thickneses of switching resistance material: 100 nm, 110 nm, 160 nm, 200 nm. Inset: scheme of connection to the single cube. Endurance cycles of the devices under SET-RESET pulse voltage scanning at 0.1 s per cycle. Each $CsPbBr_3$ nanoparticle underwent 999 cycles in a row. SEM and AFM images of each measured particle are given in Fig. S1.

memristor with a height of 150 nm is demonstrated in Fig. S2(a). Figure S2(b) shows these 1500 cycles of *I*-*V* curves measurements in a range 0–5 V. It turns out that, the nanoparticle bears about 1500 cycles under relatively wide voltage range under ambient conditions.

The cycle-to-cycle RS characteristics remain similar to each other at the same size of the cubic nanoparticle. The most optimal size for stable Set and Reset potentials is 150–160 nm $CsPbBr_3$ particles. In addition, memristors with these heights of the perovskite crystal have the

highest HRS/LRS current ratio, over 3×10^4 according to Table 1. The low power consumption is a defining feature for a memristor-based technology area. Guan et al. demonstrated that adding a ZnO layer to a W/perovskite/Al structure reduced power consumption by an order of magnitude to just 350 pW, while achieving a switching ratio of 20[44]. Notably, they also reported that illuminating the memristor with light at a power density of 2 mW/cm^2 further reduced power consumption to an impressive 25 pW. Here, the power switching can be estimated easily as $P_{SET} = I_{SET}V_{SET}$. For medium-sized perovskite nanocrystals the P_{SET} is 70–100 nW, according to Table 1. This small number of P_{SET} differs from many previous works dedicated to thin-film perovskite memristors[10,45,46]. Beside this feature, the use of a single particle-based device makes it possible to create 3D resistive random access memory devices.

To reveal the mechanism of RS, numerical simulations of the measured *I-V* curves were performed. We began our analysis by fitting the *I-V* curve for the sample with a height of 100 nm. To reproduce *I-V* curves, mobile anions and cations were accounted in the model. Electronic parameters of p-type $CsPbBr_3$ nanoparticle and barrier heights are presented in Table S1. During the modeling, anion and cation mobilities were varied to obtain the best fit with the experimental curves. The fitting shows that the anion mobility is 8×10^{-9} cm^2/Vs and the cation mobility is 4×10^{-9} cm^2/Vs, which are reasonable values for room temperatures and it is within the range (10^{-11}–10^{-8} cm^2/Vs) reported in the literature[47,48]. The resulting fitted *I-V* curves, alongside the experimental data, are presented in Fig. 3(a) and 3(b) for the 100 nm and 110 nm samples, respectively. These figures display 200 cyclic voltammograms from the experimental data compared to first six cycles from the modeling. The applied bias in these cyclic voltammograms mimics the experimental setup, utilizing a triangular pulse with rise and fall times of 50 ms. Additionally, there is a 5 ms retention time of potential following each rise and fall. This pulse potential is presented in Fig. 3(d). To calculate the *I-V* curve for the 110 nm sample, we multiplied the contact area by a correction factor of 0.83. This adjustment accounts for the asymmetry in the contact areas, as the effective area is determined by the region where the electric field is perpendicular to the spherical surface of the AFM tip within the perovskite. Consequently, this effective area may differ from the geometrical contact area.

The electrodes in the present study are inert, meaning there is no chemical reaction between the perovskite and the contacts that would lead to the injection of secondary ions. On the other hand, the perovskite is a wide band gap semiconductor with a relatively small doping level, and the concentration of the holes and electrons injected from the contacts is higher than the intrinsic carriers inside the semiconductor. In this case, the SCLC regime is realized. Moreover, the unique feature of our system is that the mobile ions concentration is significantly higher than the concentration of electron and holes and conductivity of the perovskite is primarily influenced by the accumulation of ions at the perovskite-contact interface. This ion accumulation impacts conductance through three main mechanisms. First, a strong accumulation of ions leads to significant band bending, which facilitates carrier tunneling. Second, the accumulation of ionic charges at the contact-perovskite interface reduces the Schottky barrier due to the image charge force effect induced in the contact. Third, there is an additional reduction in the Schottky barrier caused by a dipole effect. The second mechanism depends on the square root of the electric field, while the third mechanism varies linearly with the norm of electric field[49]. This distinction is crucial; without considering the third mechanism, there is a considerable discrepancy between the experimental *I-V* curve and the simulated curve. However, incorporating dipole effect modeling yields much better agreement between simulation and

Table 1 | Comparisons of the *I-V* parameters of perovskite single crystals with different size: Set/Reset current ratio, RS, HRS voltage switching, type of switching and power consumption of the switching measured as $P_{RS}=I_{SET}\times V_{SET}$.

NCs height (nm)	HRS/LRS current ratio	V_{Set} (V)	V_{Reset} (V)	Type of switching	RS consumption power (nW)
100	2500	2.2	1.4	abrupt	≈ 400
110	1200	2.0	1.4	abrupt	≈ 700
130	6700	2.3	1.3	abrupt	≈ 70
150	32000	2.7	1.3	abrupt	≈ 80
160	37000	3.5	1.1	smooth	≈ 100
200	12000	3.7	1.4	smooth	≈ 400

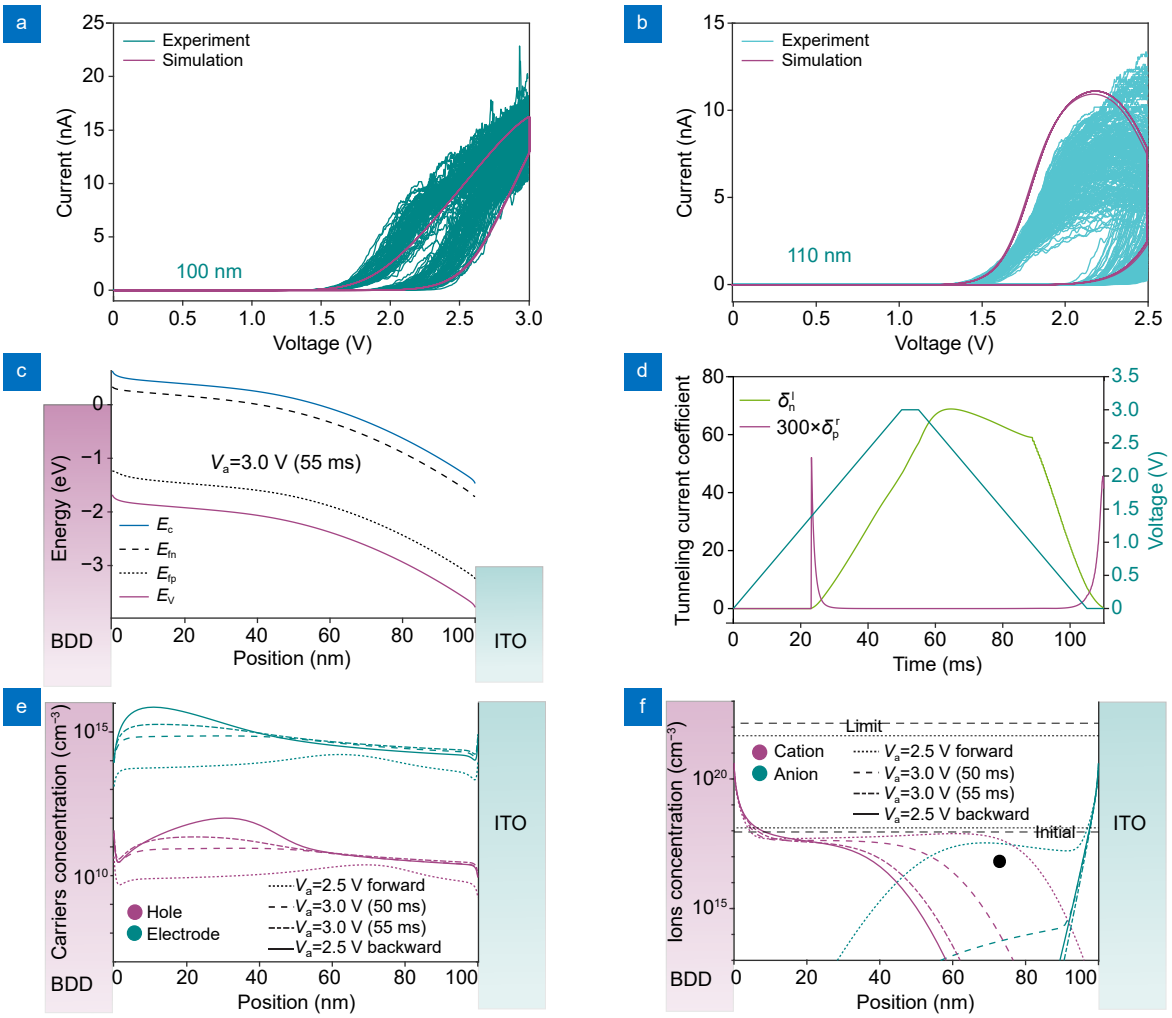

Fig. 3 | Experimental (green) and simulated (purple) *I-V* curves for (**a**) 100 nm, and (**b**) 110 nm perovskite nano-cubes. (**c**) Perovskite band diagram of 100 nm height when applied bias at ITO is 3.0 V (time = 55 ms) E_c and E_v are minimum of conduction and valence band, respectively. E_{fn} is quasi-Fermi level for electron and E_{fp} is quasi-Fermi level of holes. (**d**) Calculated tunneling coefficients for electrons from BDD (δ_n^l, green), and for holes from ITO (δ_p^r, purpure). Calculated electronic carriers (**e**), and ions (**f**), distribution inside perovskite of 100 nm height at different applied bias of V_a (green: negative carriers, purpure: positive carriers). Dashed and dotted black lines in panel (f) show initial and limiting concentration for anions and cations, respectively.

experiment. These findings highlight that in a metal-perovskite-metal structure, where electrodes are chemically inert, a fraction of accumulated ions can generate a dipole moment that significantly modifies the Schottky barrier.

When a positive bias is applied to the ITO contact, it is anticipated that anions will migrate toward the ITO contact while cations move to the BDD. It is worth to note that due to the different Schottky barriers heights at the BDD and ITO sides, the distribution of the charge carriers in the nanoparticle between the contacts will not be symmetrical. Energy level of perovskite at 3 V applied bias is illustrated in Fig. 3(c), and it effectively highlights the differences in tunneling rates between holes and electrons. Notably, the band bending is more pronounced at the BDD contact and less prevalent at the ITO, leading to a significantly higher energy barrier for hole tunneling compared to that for electron from the BDD contact. Given the pronounced difference in band bending, one would anticipate a reduced tunneling probability for holes from the ITO contact compared to electrons from the BDD. In Fig. 3(d), we present the calculated tunneling coefficients for electrons originating from the BDD contact and for holes from the ITO, depicted in green and red, respectively. Interestingly, while there is a relatively symmetrical accumulation of ions at both contacts 3(f), the tunneling coefficient for holes is over two orders of magnitude lower than that for electrons. In

contrast, the barrier lowering effects due to the image charge force (IM) and dipole effect (DE) are represented by the green and yellow dotted lines in Fig. S7 across two cycles of applied triangular bias. The total barrier lowering is indicated by the solid green line. Notably, the contribution of the dipole effect exceeds that of the image charge effect by more than a factor of two at higher applied biases. Conversely, at lower biases, their contributions are nearly equivalent. This behavior can be attributed to the dependence of barrier lowering on the magnitude of the electric field at the contact surface. As shown in Fig. S5(b), the electric field values at both the left and right contacts are similar, suggesting that the barrier lowering should also be comparable at the right contact. It is important to note that these two effects contributing to barrier lowering are mathematically described by Eq. (S5). In this equation, we utilized fitting parameters β and Γ, with values of 1.25 nm for Γ and 0.72 for β. The parameter Γ represents the thickness of polarized ions that accumulate at the contact surface. This polarization arises from the enhanced electric field, which induces dipoles primarily within a thin layer near the contacts. This phenomenon is evident in Fig. S5(b), where the field distribution is significantly greater in this narrow region at higher applied biases. The parameter β, deviating from 1, signifies the fraction of ions that exhibit a weak dipole moment due to their distance from the intense electric field, yet still contribute meaningfully to the formation of image charges at the contacts.

Figure 3(e) shows electron and hole distribution inside the perovskite at elevated applied bias. Although the density of electronic carriers is several orders of magnitude lower than that of ionic carriers at the interfaces, it is noteworthy that the peak accumulation of both electrons and holes occurs away from the interfaces. Specifically, at higher applied biases, electronic carriers localization is predominantly observed near the BDD contact (left of figure at position of zero) connected to the ground. Understanding this distribution of charge carriers is crucial for optimizing the design of ionic-electronic photo-emitters and -detectors.

The nature of the observed *I-V* curves hysteresis can be understood by analyzing Fig. 3(e). It illustrates that electron concentrations rises near the BDD contact when the applied potential to the right contact is reduced from 3 V to 2.5 V. While it is true that electronic carriers typically exhibit higher mobility, the observed increase in concentration in this context is primarily attributed to the sluggish response of ionic carriers to the applied bias. This slow response is a result of their limited mobility, which affects the overall dynamics of charge carrier distribution in the system. Detailed temporal distributions of electric field, energy levels, and carriers concentrations are presented and discussed in Section S3.6 of SI.

Memory aspect of the nano-crystal

To illustrate the memory characteristics of the nanocrystal, we utilized a crystal with a height of 100 nm and calculated the retention time by applying a triangular write pulse lasting 20 ms, immediately following a read pulse at the same scan rate. The amplitudes for the write and read pulses were set at 4 V and 2 V, respectively. Subsequently, we introduced an additional read pulse after the write pulse, varying the delay time between them. The results of this analysis are presented in Fig. 4(a, b) and Fig. S11. From these figures, it is evident that the first read pulse does not generate any output current signal. However, the write pulse produces a current pulse with an amplitude of ~5 nA. In Fig. 4(a), with no delay between the write and read pulses, the read pulse elicits a current response of ~2 nA. When the delay time is increased to 10 ms, as it is depicted in panel of Fig. 4(b), the current pulse is completely vanished. These numerical results suggest that this memory system is volatile, making it suitable for applications involving temporal information processing.

Given that this memristor exhibits volatile behavior, it is unnecessary to apply a negative pulsed potential to switch the state of the memristor from LRS to the HRS. Instead, the transition can be effectively managed by introducing an appropriate delay time between two sets of write pulses. This method simplifies the switching process and eliminates the need for an additional erase pulse. As illustrated in Fig. 4(c), we can observe two distinct sets of write and read pulses, with a calculated time delay of 13 ms between them. This delay plays a crucial role in facilitating the state transition, acting as a substitute for the traditional erase pulse. By optimizing this timing, that depends on the amplitude and duration of the pulses, one can enhance the reliability and efficiency of the memristor's operation, ensuring a seamless transition between states while maintaining data integrity. This approach not only simplify the switching mechanism but also contributes to improved overall performance in memory applications.

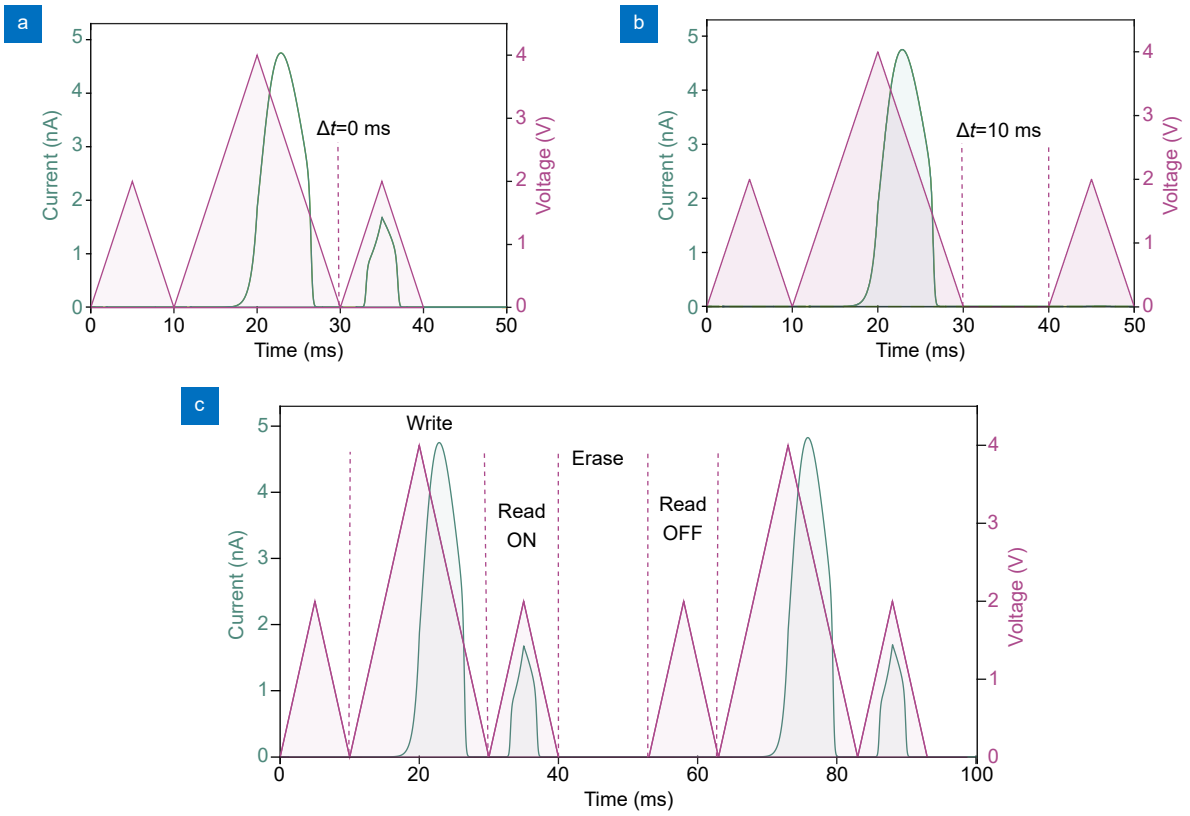

Fig. 4 | Memory logic and retention time calculation of the 100 nm perovskite crystal. Time delay between high amplitude (4 V) and low amplitude (2 V) triangle pulse is (**a**) zero, and (**b**) 10 ms. (**c**) Write, read and erase logic with write pulse duration of 20 ms, read pulse duration of 10 ms and erase time of 13 ms.

Conclusions

In this study, we have successfully synthesized single $CsPbBr_3$ perovskite nanocrystals on an ITO substrate which act as unipolar nanomemristors. By using inert boron-doped-diamond probe as a top nanocontact, cyclic *I-V* curves measurement were performed for single nanoparticles. The measurements reveal a strong unipolar hysteresis of the *I-V* curves, where the HRS/LRS current ratio reaches 3×10^4. HRS/LRS ratio and V_{set} voltage are increased with the increase of the nanoparticle height (100–250 nm range). The HRS/LRS switching behavior depends on the size of the nano-crystals: smaller crystals exhibit abrupt switching of a sub-10-ms, while crystals with hight above 150 nm show smoother transitions. The studied nanocrystals bear more than 1500 cycles of the *I-V* curves measurement in a 0–5 V range of atmospheric ambient conditions. Moreover, after one month storage in the same conditions nanomemristors show the same stable cycling. The connection by chemically inert contacts reveal a Schottky barrier height modulation as a main mechanism of the resistive switching. In addition to barrier reduction through image charge force, our calculations indicate that the dipole effect caused by ions, significantly contributes to barrier reduction through dipole effect. The volatile memory response has been modeled, showing perspectives for the temporal signal processing. This study represents a significant advancement in our understanding of resistive state switching in perovskite memristors and highlights single $CsPbBr_3$ perovskite nanomemristors as perspective object for further studies of ultracompact neuromorphic computing systems.

Methods

Perovskite nanocrystals synthesis and analysis

The perovskite synthesis of $CsPbBr_3$ NCs were synthesised using a similar procedure as described by Tiguntseva et al.[25]. Clean from general contamination ITO glass (Kaivo, 7 Ohm/sq) was used as a bottom contact. Perovskite NCs were obtained in two steps: $PbBr_2$ DMF solution (62.34 mg/mL) were spin-coated at 2500 rpm for 40 second and then placed on hot plate at 75 °C for 30 minutes. Then $PbBr_2$ films were transferred to CsBr solution in methanol (7.5 mg/mL) for 10 minutes at 50 °C

to initiate perovskite formation and crystallized at 150 °C.

A scanning electron microscope (SEM) Merlin (Carl Zeiss) was used for SEM imaging. Perovskite cubes position on ITO was determined with use of low accelerating voltage of 1.5 kV to prevent charge effects. In-Lens detector was chosen to obtain better topography resolution. The working distance was about 4.4 mm.

Raman spectroscopy was performed under CW-laser radiation (HNL100LB, Thorlabs, output power 10 mW), which was focused using a micro-objective lens (M Plan Apo HR, Mitutoyo, M = ×100, NA = 0.90), in the focal plane of which there was a glass substrate with perovskite microcrystals. The interaction result of focused radiation with semiconductors generated a Raman scattering signal collected by the same micro-objective lens. This is the principle of measurement in geometry on reflection. A long-pass dichroic mirror with a cutoff wavelength of 650 nm was used to separate the radiation of the information signal from the excitation. Next, the information signal was sent to a commercial spectrometer (Horiba Jobin-Yvon LabRam HR800 with diffraction grating support of 600 lines per mm) to decompose the optical signal into a spectrum and detect it with a camera (water-cooled CCD detector iDus DU420A-OE, Andor). A configurable pinhole is installed at the input of the spectrometer, which is why the resulting microscopic system is confocal and allows to capture a signal from a spatially limited area. The measurements were carried out at room temperature (294 K) in atmospheric ambient condition.

I-V analysis

Measurement of the *I-V* curves was performed by conductive AFM using Ntegra Aura (NT-MDT) scanning probe microscope. Commercial DCP30 (Tipsnano) probes with a BDD conductive coating were used as a top contact. The tip curvature radius of the probes was 100–200 nm and a cantilever stiffness were of ∼60 N/m. The height of the measured particles was estimated from the AFM image obtained in the semi-contact mode. For stable electrical contact, the probe's pressure force was of 300 nN. The second electrical contact was connected to the particle-free ITO surface with a spring probe pin. *I-V* curves were measured by applying a voltage to the substrate and registering the current by the amperemeter at the probe's side. The sensitivity of the amperemeter was 3 pA. The minimal time for the *I-V* curve measurement with both voltage ascending and descending directions was of 50 ms with a time step between the measurement points of 0.05 ms.

Modeling part

To analyze the experimental *I-V* curves, we employed a one-dimensional (1D) ionic-electronic drift-diffusion (DD) model in transient condition. Given the asymmetry of the electrodes and the larger area of the bottom electrode in relation to the perovskite crystal size, we focused on two nanocrystals with heights of 100 nm and 110 nm. These crystals have a relatively small volume-to-surface ratio, ensuring that the area of the bottom electrode is not excessively larger than that of the top electrode, which allows us to effectively utilize the 1D model. Several open-source code for the 1D ionic-electronic DD model has been developed by various authors[50–52]. However, these publications do not consider the effects of charge carrier tunneling and Schottky barrier reduction effect at the perovskite-contacts interface.

Since ions cannot be extracted or injected from the electrodes, they tend to accumulate at the perovskite-electrode interface by applying of a voltage bias on the contacts, resulting in significant alterations to the electric potential that can induces numerical instability. To address this, we employ the well-known Scharfetter-Gummel (SG) discretization for current fluxes. While applying SG discretization to the electronic carrier current density using the Boltzmann distribution is straightforward[53], we adapted a modified scheme of SG discretization for ionic carriers as proposed by Koprucki et al.[54]. They modified the original SG scheme by incorporating a diffusion enhancement approach and an inverse activity coefficient. In a other work by Farrell[55], it is shown that the error associated with the diffusion enhancement approach is consistently lower than that of the second approach across a broader range of varying potentials V and electro-chemical potentials η in a typical grid, as analyzed through the finite volume method. The discrete from of current density for electronic and ionic carriers using SG discretization are represented in the Section S3.4 of Supplementary information.

Using the simulation parameters outlined in Table S1 of the SI and employing SG discretization to solve the PDEs represented by Eqs. S1–S5, we first determined the equilibrium condition for electronic carriers by assuming zero mobility for ionic carriers. This equilibrium solution served as the initial guess for addressing the non-equilibrium scenario with initially uniformly distributed

fixed ions. These fixed ions is introduced to effectively model Schottky defects within the system[50]. We also initialized the distribution of mobile ions to match that of the fixed ions. For solving the PDEs, we utilized a combination of the Gummel and Newton methods, leveraging the solution from the previous time step as the starting point for the current step. Given the nonlinear nature of the PDEs, we implemented a dynamic damping strategy as proposed by Amrein et al.[56]. The solver parameters for the damped Newton method, including the initial Gummel iteration prior to applying the Newton method, are detailed in Table S2 of the SI.

References

1. Wei HD, Chu L. Two-dimensional halide perovskite memristor arrays: linearly programmable for neuromorphic computing. *Sci China Mater* **68**, 1678–1679 (2025).
2. Gong JQ, Ji SL, Li JT et al. Three-dimensional/one-dimensional perovskite heterostructures for stable tri-state synaptic memristors. *Sci China Mater* **67**, 2848–2855 (2024).
3. Dutta M, Brivio S, Spiga S. Unraveling the roles of switching and relaxation times in volatile electrochemical memristors to mimic neuromorphic dynamical features. *Adv Electron Mater* **10**, 2400221 (2024).
4. Yan XB, Zhang ZX, Guan ZY et al. A high-speed true random number generator based on Ag/SiN_x/n-Si memristor. *Front Phys* **19**, 13202 (2024).
5. Xie ZW, Jiang K, Zhang SL et al. Nonvolatile and reconfigurable two-terminal electro-optic duplex memristor based on III-nitride semiconductors. *Light Sci Appl* **13**, 78 (2024).
6. Liu ZH, Cheng PP, Li YF et al. Multilevel halide perovskite memristors based on optical & electrical resistive switching effects. *Mater Chem Phys* **288**, 126393 (2022).
7. Zhao XN, Wang ZQ, Li WT et al. Photoassisted electroforming method for reliable low-power organic-inorganic perovskite memristors. *Adv Funct Mater* **30**, 1910151 (2020).
8. Wang H, Yang JL, Yang Z et al. Optical-electrical coordinately modulated memristor based on 2D ferroelectric RP perovskite for artificial vision applications. *Adv Sci* **11**, 2403150 (2024).
9. Xing J, Zhao C, Zou YT et al. Modulating the optical and electrical properties of $MAPbBr_3$ single crystals via voltage regulation engineering and application in memristors. *Light Sci Appl* **9**, 111 (2020).
10. Pérez-Martínez JC, Berruet M, Gonzales C et al. Role of metal contacts on halide perovskite memristors. *Adv Funct Mater* **33**, 2305211 (2023).
11. Gonzales C, Guerrero A. Mechanistic and kinetic analysis of perovskite memristors with buffer layers: the case of a two-step set process. *J Phys Chem Lett* **14**, 1395–1402 (2023).
12. Sawa A. Resistive switching in transition metal oxides. *Mater Today* **11**, 28–36 (2008).
13. Yantara N, Mathews N. Toolsets for assessing ionic migration in halide perovskites. *Joule* **8**, 1239–1273 (2024).
14. Hussain T, Fatima K, Anjum A et al. Experimental evidence of ion migration in aged inorganic perovskite solar cells using non-destructive RBS depth profiling. *Mater Adv* **3**, 7846–7853 (2022).
15. Kamat PV, Kuno M. Halide ion migration in perovskite nanocrystals and nanostructures. *Acc Chem Res* **54**, 520–531 (2021).
16. Satapathi S, Raj K, Yukta et al. Halide-perovskite-based memristor devices and their application in neuromorphic computing. *Phys Rev Appl* **18**, 017001 (2022).
17. Guan XW, Hu WJ, Haque MA et al. Light-responsive ion-redistribution-induced resistive switching in hybrid perovskite Schottky junctions. *Adv Funct Mater* **28**, 1704665 (2018).
18. Han JS, van Le Q, Choi J et al. Lead-free all-inorganic cesium tin iodide perovskite for filamentary and interface-type resistive switching toward environment-friendly and temperature-tolerant nonvolatile memories. *ACS Appl Mater Interfaces* **11**, 8155–8163 (2019).
19. Emelianov NA, Ozerova VV, Fedotov YS et al. Direct nanoscale visualization of the electric-field-induced aging dynamics of $MAPbI_3$ thin films. *Materials* **16**, 4277 (2023).
20. Elnaggar M, Boldyreva AG, Elshobaki M et al. Decoupling contributions of charge-transport interlayers to light-induced degradation of p-i-n perovskite solar cells. *Solar RRL* **4**, 2000191 (2020).
21. Yang JL, Kelly TL. Decomposition and cell failure mechanisms in lead halide perovskite solar cells. *Inorg Chem* **56**, 92–101 (2017).
22. Liu J, Yang FX, Cao LL et al. A robust nonvolatile resistive memory device based on a freestanding ultrathin 2D imine polymer film. *Adv Mater* **31**, 1902264 (2019).
23. Divitini G, Cacovich S, Matteocci F et al. *In situ* observation of heat-induced degradation of perovskite solar cells. *Nat Energy* **1**, 15012 (2016).
24. Yoo EJ, Lyu M, Yun JH et al. Resistive switching behavior in organic-inorganic hybrid $CH_3NH_3PbI_{3-x}Cl_x$ perovskite for resistive random access memory devices. *Adv Mater* **27**, 6170–6175 (2015).
25. Tiguntseva E, Koshelev K, Furasova A et al. Room-temperature lasing from Mie-resonant nonplasmonic nanoparticles. *ACS Nano* **14**, 8149–8156 (2020).
26. Rodová M, Brožek J, Knížek K et al. Phase transitions in ternary caesium lead bromide. *J Therm Anal Calorim* **71**, 667–673 (2003).
27. Pradhan N. $CsPbBr_3$ perovskite nanocrystals: linking orthorhombic structure to cubic geometry through atomic models and HRTEM analysis. *ACS Energy Lett* **10**, 1057–1061 (2025).
28. Liao ML, Shan BB, Li M. In situ Raman spectroscopic studies of thermal stability of all-inorganic cesium lead halide ($CsPbX_3$, X= Cl, Br, I) perovskite nanocrystals. *J Phys Chem Lett* **10**, 1217–1225 (2019).
29. Aebli M, Benin BM, McCall KM et al. White $CsPbBr_3$: characterizing the one-dimensional cesium lead bromide polymorph. *Helv Chim Acta* **103**, e2000080 (2020).
30. Svirskas Š, Balčiūnas S, Šimėnas M et al. Phase transitions, screening and dielectric response of $CsPbBr_3$. *J Mater Chem A* **8**, 14015–14022 (2020).
31. Khalid A, Alanazi AM, Alderhami SA et al. Impact of metallic and vacancy-oriented filamentary switching on memristor device based on $Cs_2AgInCl_6$ double halide perovskite. *Mater Sci Semicon Proc* **165**, 107678 (2023).
32. Im IH, Baek JH, Kim SJ et al. Halide perovskites-based diffusive memristors for artificial mechano-nociceptive system. *Adv Mater* **36**, 2307334 (2024).

33. Zhu YY, Cheng PW, Shi J et al. Bromine vacancy redistribution and metallic-ion-migration-induced air-stable resistive switching behavior in all-inorganic perovskite $CsPbBr_3$ film-based memory device. *Adv Electron Mater* **6**, 1900754 (2020).
34. Xu J, Wu YH, Li ZZ et al. Resistive switching in nonperovskite-phase $CsPbI_3$ film-based memory devices. *ACS Appl Mater Interfaces* **12**, 9409–9420 (2020).
35. Li A, Wang ZQ, Peng Z et al. Improvement in stability and storage performance of all-inorganic perovskite $CsPb(Br_{1-x}I_x)_3$ memristors based on simple halide ion migration. *ACS Appl Electron Mater* **6**, 3801–3809 (2024).
36. Zhou FC, Liu YH, Shen XP et al. Low-voltage, optoelectronic $CH_3NH_3PbI_{3-x}Cl_x$ memory with integrated sensing and logic operations. *Adv Funct Mater* **28**, 1800080 (2018).
37. Yang KY, Li FS, Veeramalai CP et al. A facile synthesis of $CH_3NH_3PbBr_3$ perovskite quantum dots and their application in flexible nonvolatile memory. *Appl Phys Lett* **110**, 083102 (2017).
38. Doan UTT, Le DK, Huynh TL et al. Tuned transport path of perovskite $MAPbI_3$-based memristor structure. *ChemPhysChem* **24**, e202300210 (2023).
39. Ma HL, Wang W, Xu HY et al. Interface state-induced negative differential resistance observed in hybrid perovskite resistive switching memory. *ACS Appl Mater Interfaces* **10**, 21755–21763 (2018).
40. Berruet M, Pérez-Martínez JC, Romero B et al. Physical model for the current-voltage hysteresis and impedance of halide perovskite memristors. *ACS Energy Lett* **7**, 1214–1222 (2022).
41. Kim H, Kim JS, Choi J et al. $MAPbBr_3$ halide perovskite-based resistive random-access memories using electron transport layers for long endurance cycles and retention time. *ACS Appl Mater Interfaces* **16**, 2457–2466 (2024).
42. Yin YL, Yao ZY, Xia Y et al. A method to improve the performance of all-inorganic halide perovskite $CsPbBr_3$ memory. *Mater Res Express* **9**, 065007 (2022).
43. Kinoshita K, Tsunoda K, Sato Y et al. Reduction in the reset current in a resistive random access memory consisting of NiO_x brought about by reducing a parasitic capacitance. *Appl Phys Lett* **93**, 033506 (2008).
44. Guan H, Sha J, Zhang ZJ et al. Optical and oxide modification of CsFAMAPbIBr memristor achieving low power consumption. *J Alloy Compd* **891**, 162096 (2022).
45. Gu C, Lee J S. Flexible hybrid organic–inorganic perovskite memory. *ACS Nano* **10**, 5413–5418 (2016).
46. Wang YC, Xiong YX, Sha J et al. Inverse photoconductivity effect in triple cation organic-inorganic hybrid perovskite memristors with various iodine concentrations, electrodes, and modified layers. *J Mater Chem C* **10**, 1414–1420 (2022).
47. Pan DX, Fu YP, Chen J et al. Visualization and studies of ion-diffusion kinetics in cesium lead bromide perovskite nanowires. *Nano Lett* **18**, 1807–1813 (2018).
48. Shewmon NT, Yu H, Constantinou I et al. Formation of perovskite heterostructures by ion exchange. *ACS Appl Mater Interfaces* **8**, 33273–33279 (2016).
49. Sze SM, Li YM, Ng KK. *Physics of Semiconductor Devices* 4th ed (John Wiley & Sons, 2021).
50. Calado P, Gelmetti I, Hilton B et al. Driftfusion: an open source code for simulating ordered semiconductor devices with mixed ionic-electronic conducting materials in one dimension. *J Comput Electron* **21**, 960–991 (2022).
51. Clarke W, Bennett LJ, Grudeva Y et al. IonMonger 2.0: software for free, fast and versatile simulation of current, voltage and impedance response of planar perovskite solar cells. *J Comput Electron* **22**, 364–382 (2023).
52. Courtier NE, Cave JM, Walker AB et al. Ionmonger: a free and fast planar perovskite solar cell simulator with coupled ion vacancy and charge carrier dynamics. *J Comput Electron* **18**, 1435–1449 (2019).
53. Mahmoodpoor A, Makarov S. Numerical analysis of charge carriers injection in a light emitter or detector device based on a metal-semiconductor-metal structure. *Photonics Nanostruct Funda Appl* **58**, 101213 (2024).
54. Koprucki T, Gärtner K. Discretization scheme for drift-diffusion equations with strong diffusion enhancement. *Opt Quant Electron* **45**, 791–796 (2013).
55. Farrell P, Patriarca M, Fuhrmann J et al. Comparison of thermodynamically consistent charge carrier flux discretizations for Fermi-Dirac and Gauss-Fermi statistics. *Opt Quant Electron* **50**, 101 (2018).
56. Amrein M, Wihler TP. An adaptive Newton-method based on a dynamical systems approach. *Commun Nonlinear Sci Numer Simul* **19**, 2958–2973 (2014).

Acknowledgements

This work was supported by the Russian Science Foundation (project number 24-62-00022) for data analysis and by Priority 2030 Federal Academic Leadership Program for samples synthesis.

Competing interests

The authors declare no competing financial interests.

Supplementary information

Supplementary information for this paper is available at https://doi.org/10.29026/oea.2025.250110

Scan for Article PDF